LETTER

doi:10.1038/nature12237

A micrometre-scale Raman silicon laser with a microwatt threshold

Yasushi Takahashi[1,2], Yoshitaka Inui[3], Masahiro Chihara[1], Takashi Asano[3], Ryo Terawaki[1] & Susumu Noda[3,4]

The application of novel technologies to silicon electronics has been intensively studied with a view to overcoming the physical limitations of Moore's law, that is, the observation that the number of components on integrated chips tends to double every two years. For example, silicon devices have enormous potential for photonic integrated circuits on chips compatible with complementary metal–oxide–semiconductor devices, with various key elements having been demonstrated in the past decade[1–6]. In particular, a focus on the exploitation of the Raman effect has added active optical functionality to pure silicon[7–10], culminating in the realization of a continuous-wave all-silicon laser[11]. This achievement is an important step towards silicon photonics, but the desired miniaturization to micrometre dimensions and the reduction of the threshold for laser action to microwatt powers have yet to be achieved: such lasers remain limited to centimetre-sized cavities with thresholds higher than 20 milliwatts[12], even with the assistance of reverse-biased p–i–n diodes. Here we demonstrate a continuous-wave Raman silicon laser using a photonic-crystal, high-quality-factor nanocavity without any p–i–n diodes, yielding a device with a cavity size of less than 10 micrometres and an unprecedentedly low lasing threshold of 1 microwatt. Our nanocavity design exploits the principle that the strength of light–matter interactions is proportional to the ratio of quality factor to the cavity volume and allows drastic enhancement of the Raman gain beyond that predicted theoretically[13,14]. Such a device may make it possible to construct practical silicon lasers and amplifiers for large-scale integration in photonic circuits.

In 2002, stimulated Raman scattering in rib waveguides was proposed as a novel mechanism to generate optical gain in crystalline silicon[7]. However, the Raman gain is inherently small compared with the gain due to radiative recombination in direct-bandgap semiconductors[15,16]. Therefore, Raman silicon lasers have thus far required long cavities and high excitation powers to generate net gain. Furthermore, free carrier absorption (FCA) induced by two-photon absorption[17,18] (TPA) has a superlinear dependence on the excitation power, resulting in additional losses that compete with the Raman gain. The incorporation of reverse-biased p–i–n diodes along the waveguides has also been necessary to remove the carriers[10–12]. To overcome all these disadvantages, the design of optical cavities with high quality factors (Q) and small volumes (V) is essential because high Q/V ratios yield strong light–matter interactions and enhance the Raman gain. From this point of view, the use of high-Q, photonic-crystal nanocavities[19–23] is desirable. However, there have thus far been no experimental reports of stimulated Raman scattering in nanocavities and no feasible designs have been proposed for cavities in which continuous-wave lasing can be achieved. Progress in this area of research halted after a number of numerical studies on elementary cavity structures were unsuccessful in finding a design in which Raman emission can be detected[13,14,24]. However, we now present a laser design that incorporates a heterostructure nanocavity, and demonstrate that it exhibits lasing with an unprecedentedly ultralow threshold of 1 μW.

Figure 1a–c illustrates the basic features of the nanocavity Raman laser developed in this study. The photonic crystal has the well-known triangular lattice structure formed by circular air holes in a suspended silicon membrane. The heterostructure nanocavity is formed from a line-defect waveguide (Fig. 1d). This waveguide has two types of propagation mode within the photonic bandgap, an odd-waveguide mode and an even-waveguide mode. The low-loss propagation bands of these modes are shown in Fig. 1e. The modes are classified as 'odd' or 'even' by the symmetry of the electric field E_y, as schematically displayed. The corresponding band structure in wavenumber (k)-space is shown in Fig. 1f, where the blue and red curves show the dispersion relations for the odd-waveguide mode and even-waveguide mode, respectively. The dashed line represents the light line, below which the low-loss propagations are obtained (Supplementary Information, section A). The nanocavity is formed by a small increase (Δa) of the lattice constant in a short section of the waveguide, which moves the dispersion relation curves to a lower frequency. Accordingly, the frequency of the odd- and even-waveguide bands is lowered in this section[21] (Fig. 1b), such that 'odd' and 'even' nanocavity modes are formed as a result of optical confinement by the mode-gap differences. (The mode gap is the frequency range with no low-loss waveguide modes.) In our Raman laser, we use these nanocavity modes to confine pump light and Stokes-Raman-scattered light, respectively (Fig. 1c).

Figure 1g shows the calculated x and y components of the electric field distribution of the odd nanocavity mode, which are denoted E_{x_pump} and E_{y_pump}, respectively. Figure 1h presents the analogous electric field distributions of the even nanocavity mode, denoted E_{x_Raman} and E_{y_Raman}. The E_{x_pump} and E_{x_Raman} distributions have different parities because they are generated from different waveguide modes. This is also the case for E_{y_pump} and E_{y_Raman}. Such pairs of modes initially seem unsuitable for Raman lasers owing to the small degree of overlap for stimulated Raman scattering. However, it can be seen from Fig. 1g, h that the 'cross components', E_{x_pump} and E_{y_Raman} (and E_{y_pump} and E_{x_Raman}), have the same line symmetry and similar distributions. This is a key observation, showing that the problem of cavity design can be solved by carefully selecting the crystallographic direction in which the nanocavity is formed, as discussed below. We will next demonstrate that the frequencies (f_p and f_R), Q values (Q_p and Q_R), modal volumes (V_p and V_R) and electric field distributions (E_p and E_R) associated with this unusual pair of modes allow dramatic enhancement of the Raman gain.

The first advantage of our design is that the frequency spacing ($\Delta f = f_\mathrm{p} - f_\mathrm{R}$) between these nanocavity modes can be tuned to the silicon Raman shift of 15.6 THz by changing the air-hole radius. This is because the electric field densities of the two modes within the air holes are fundamentally unequal owing to the difference in parity. It is fortuitous that the frequency spacing is close to 15.6 THz when the lattice constant (a) is set so that the even nanocavity mode has an operation wavelength in the telecommunications band between 1.30 and 1.60 μm. Tuning the frequency spacing to exactly 15.6 THz is

[1]Nanoscience and Nanotechnology Research Center, Research Organization for the 21st Century, Osaka Prefecture University, Sakai, Osaka 599-8570, Japan. [2]Japan Science and Technology Agency, PRESTO, Kawaguchi, Saitama 332-0012, Japan. [3]Department of Electronic Science and Engineering, Kyoto University, Kyoto 615-8510, Japan. [4]Photonics and Electronics Science and Engineering Center, Kyoto University, Kyoto 615-8510, Japan.

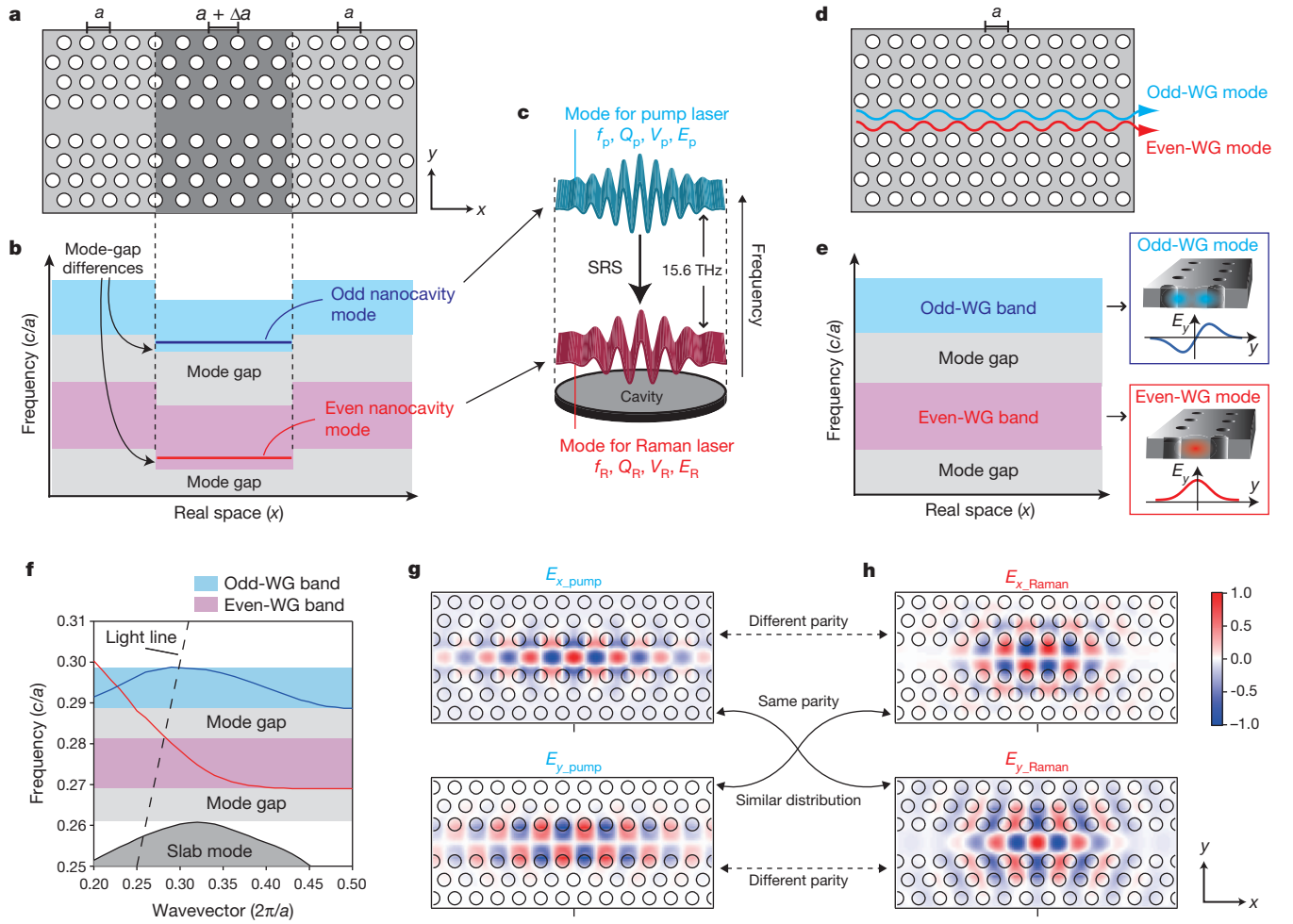

Figure 1 | Structure of Raman silicon laser based on a heterostructure nanocavity. **a**, Schematic picture of the heterostructure nanocavity in the photonic crystal slab. The lattice constant at the centre of the cavity is slightly larger in the *x* direction. **b**, Band diagram of the nanocavity along the *x* direction, where *c* is the speed of light in vacuum. Two high-*Q* nanocavity modes originating from odd- and even-waveguide modes are formed in the heterostructure. **c**, Configuration of Raman silicon laser using a small cavity. The two nanocavity modes in **b** are used to confine pump light and Stokes-Raman-scattered light, respectively. SRS, stimulated Raman scattering. **d**, Line-defect waveguide formed by a missing row of air holes, in which two propagating waveguide modes are formed. WG, waveguide. **e**, Band diagram of the line-defect waveguide. The insets sketch the profiles of the propagating modes. **f**, Calculated band structure for the line-defect waveguide in *k*-space. **g**, **h**, Calculated electric field distributions for the odd nanocavity mode and the even nanocavity mode, respectively. The colour scale represents the intensity of the electric field.

essential for the efficient generation of Raman scattered light into the even nanocavity mode, and the flexibility of our design is thus an advantage over the alternatives[13,14,24].

Second, although the *Q* factor of the even nanocavity mode (Q_R) can be made as high as 4,000,000 in heterostructure nanocavities[23], the odd nanocavity mode has so far received little attention regarding its possible use as a high-*Q* resonant mode. However, we will show below that the *Q* factor of this mode (Q_p) can be higher than 100,000 in heterostructure nanocavities. Because the laser threshold is inversely proportional to the product of Q_p and Q_R, owing to the reduction of cavity loss, the characteristic of high *Q* factors for both modes is another advantage of our design. Below we demonstrate experimentally that the product Q_pQ_R can exceed 10^{11}, which is 10,000 times higher than previously reported values[13,14]. In addition, the cavity volumes of both modes (V_p and V_R) can be reduced to a cubic wavelength when Δf is at the desired value and Q_pQ_R is high. This volume is 10,000 times smaller than in earlier rib-waveguide Raman lasers[11,12]. Therefore, our design enables extraordinarily high Q_pQ_R/V ratios, which no cavity design reported thus far has been able to achieve.

Last, our design allows high effective overlap for the Raman gain because the nanocavity is fabricated along a unique crystallographic direction of the silicon-on-insulator (SOI) substrate, which further enhances the advantages discussed above. If the device is fabricated on a standard (001) SOI, then either the [100] or [110] direction can be chosen as the *x* axis of the nanocavity. Considering the Raman selection rules in silicon and that both nanocavity modes have transverse electric polarization with respect to the slab, in our design the Raman gain in each direction is as follows, where an asterisk denotes complex conjugate (Supplementary Information, section B):

$$G_{[100]} \propto \iiint_{Si} \left|E^*_{x\_Raman}E_{y\_pump} + E^*_{y\_Raman}E_{x\_pump}\right|^2 \mathrm{d}x\,\mathrm{d}y\,\mathrm{d}z \quad (1)$$

$$G_{[110]} \propto \iiint_{Si} \left|E^*_{x\_Raman}E_{x\_pump} - E^*_{y\_Raman}E_{y\_pump}\right|^2 \mathrm{d}x\,\mathrm{d}y\,\mathrm{d}z \quad (2)$$

Usually, SOI-based photonics devices are fabricated along [110] or its equivalent directions because the wafer is easily cleaved along [110]. The previously reported rib-waveguide lasers were indeed designed along [110] (refs 9–12) and the previous theoretical studies used the same direction[14,24]. Although the Δf and *Q* factors are insensitive to the direction of fabrication, equation (1) indicates that the Raman gain will be higher for the [100] direction because there is a negative term in equation (2). The overlap involving the cross components is significant

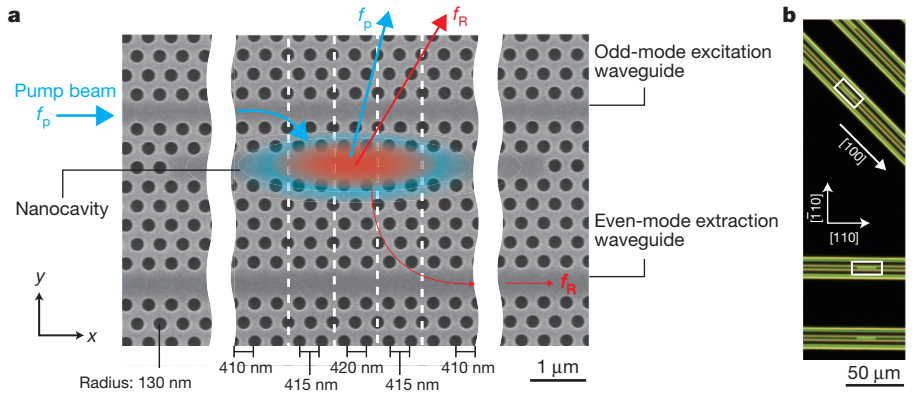

Figure 2 | Configuration of nanocavity Raman silicon laser. **a**, Scanning electron microscope image of the core region of the laser. The annotations show how laser light created from the pump beam is mainly emitted in the direction vertical to the slab. We refer to this as dropped light. A portion of the light is propagated along the even-mode extraction waveguide. **b**, Dark-field microscope image of the fabricated chip. Nanocavities oriented along [100] and [110] were fabricated. Patterned and unpatterned regions are clearly distinguishable. The rectangles indicate the areas shown in **a**.

in equation (1), which involves the odd and even nanocavity modes with the desirable parities and distributions indicated in Fig. 1g, h. Consequently, our design is also superior in terms of overlap and can drastically enhance the Raman gain when the device is fabricated along [100].

We now demonstrate the operation of a device fabricated according to our design strategy. Figure 2a shows a scanning electron microscope image of a nanocavity formed using well-established silicon nanofabrication technologies[25]. The central line defect is the heterostructure nanocavity, and the upper and lower line defects are waveguides used to pump the odd nanocavity mode and to extract Raman laser light from the even nanocavity mode, respectively. The structural parameters were chosen such that the even nanocavity mode has a wavelength in the 1.55-μm band: the lattice constant is $a = 410$ nm, the air-hole radius is $r = 130$ nm, the silicon slab thickness is 220 nm and there are two successive 5-nm increases of a in the x direction. Figure 2b shows a microscope image of the chip. We also fabricated a nanocavity along [110] for reference. We note that no p–i–n diodes to reduce the TPA-induced FCA were incorporated.

We investigated the optical properties using the measurement set-up shown in Fig. 3a. Figure 3b, c show the measured resonant spectra of the two nanocavity modes for a sample with the x axis aligned to [100]. The even nanocavity mode was excited through the even-mode extraction waveguide. The linewidth ($\Delta\lambda$) of the odd nanocavity mode peak is 13.7 pm at the resonant wavelength $\lambda_p = 1424.99$ nm. A Q_p value of 104,000 is obtained from the relation $Q = \lambda/\Delta\lambda$. The Q_R value for the even nanocavity mode is estimated as 1,400,000 at the resonant wavelength $\lambda_R = 1540.13$ nm, and, thus, $Q_pQ_R = 1.5 \times 10^{11}$. The frequency spacing is $\Delta f = c(1/\lambda_p - 1/\lambda_R) = 15.74$ THz, which is not exactly matched to the silicon Raman shift of 15.6 THz.

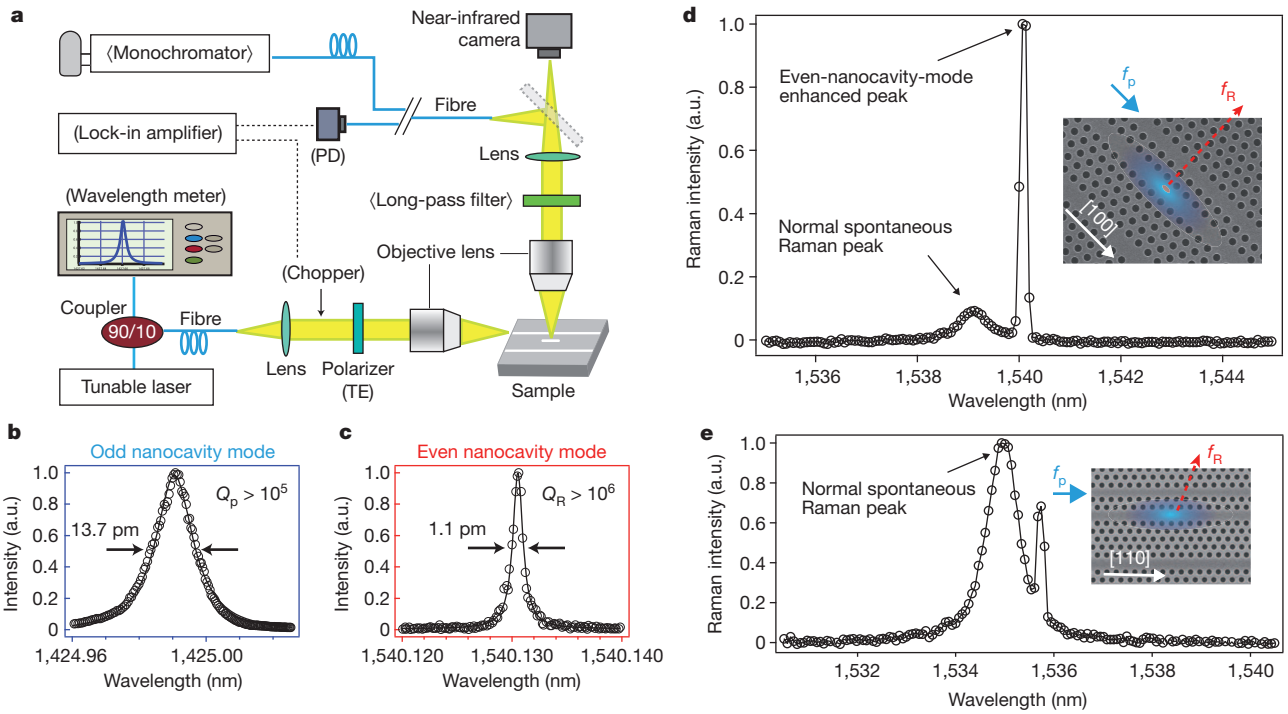

Figure 3 | Optical measurements on fabricated nanocavities. **a**, Set-up used to obtain resonant spectra and Raman-scattering spectra. The components enclosed in parentheses and angle brackets were used for resonant spectra and Raman spectra, respectively. TE, transverse electric. **b**, **c**, Resonant spectra for odd (**b**) and even (**c**) nanocavity modes. a.u., arbitrary units. **d**, Raman spectrum for the [100] nanocavity, measured while pumping the odd nanocavity mode in **b** with an input power of 1 μW. **e**, Raman spectrum for the reference [110] nanocavity. The resolution limit of the monochromator is ~100 pm.

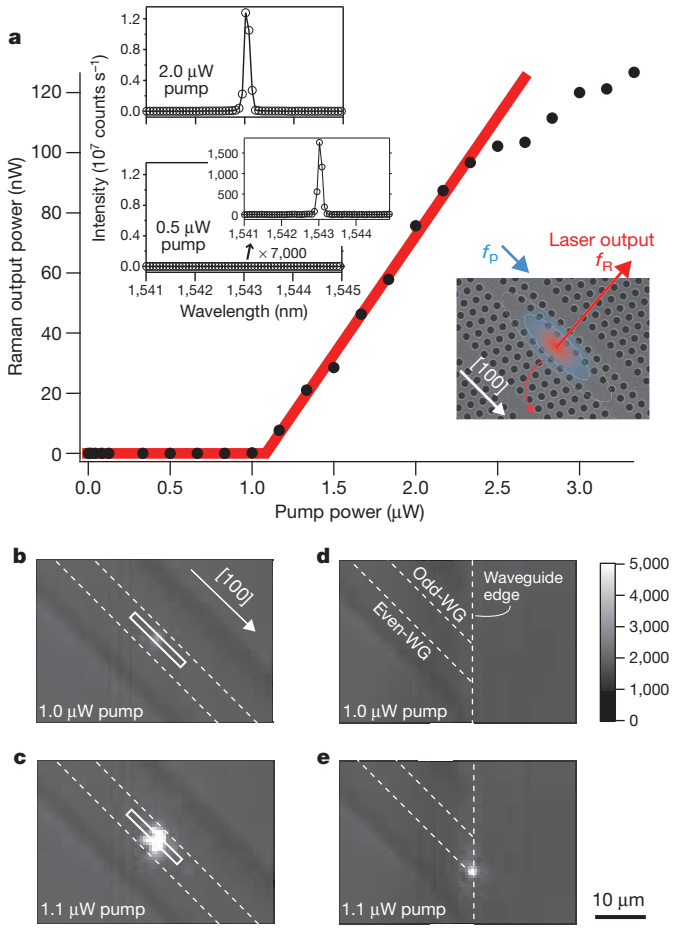

Figure 4 | Continuous-wave operation of fabricated nanocavity Raman silicon laser. a, Laser output power (black points) as a function of pump power coupled into the nanocavity. The absolute power was estimated from the dropped-light intensity, taking into account the loss from the experimental set-up. The red line shows the output of a typical laser with a slope efficiency of 8% above threshold. The insets show the Raman spectra below and above the threshold power on the same scale, demonstrating Raman laser action. **b**, **c**, Near-infrared camera images of the nanocavity Raman laser below and above the threshold, using a long-pass filter to eliminate the pump light. Dotted lines represent the waveguides. Rectangles indicate the nanocavity position. **d**, **e**, Near-infrared images at a waveguide edge. Images in **b**–**e** are shown on the same intensity scale.

Figure 3d shows the Raman scattering spectrum measured when the odd nanocavity mode in Fig. 3b was excited by a continuous-wave laser beam coupling only 1 μW of power into the cavity. Although the detuning, $\Delta f - 15.6$ THz, from the Raman shift is larger than the Raman gain width of silicon (~0.1 THz), a sharp Raman scattering peak is nevertheless observed. This is enhanced by the strong confinement of the even nanocavity mode at the tail of the normal spontaneous Raman emission peak. The linewidth of the normal spontaneous Raman peak is 750 pm, which is almost the same as the Raman gain width of silicon. As shown in Fig. 3e, the resonant peak is much smaller for the reference [110] nanocavity, which has similar Q values and Δf to the [100] nanocavity in Fig. 3d. Although the sample in Fig. 3d did not oscillate, owing to the residual mismatch of Δf, we were able to fabricate a sample with a Δf value of exactly 15.6 THz by carefully changing the radius of the air holes (Supplementary Information, section C). We separately confirmed that the rate of change of Δf with radius r is $(\partial \Delta f/\partial r) \approx 0.15\ \mathrm{THz\,nm^{-1}}$.

Finally, we present details of lasing in a sample with $Q_P = 140{,}000$, $Q_R = 1{,}500{,}000$, $\lambda_P = 1428.38$ nm and $\lambda_R = 1543.02$ nm. The laser output power is plotted in Fig. 4a as a function of the pump power coupled into the nanocavity, showing lasing oscillation above a threshold of 1 μW. This threshold is 20,000 times smaller than that previously reported for a rib-waveguide Raman silicon laser[12] and is also smaller than predicted by numerical studies[13,14]. The spectral peak intensities in the insets indicate that the efficiency for Raman light generation above threshold is more than 1,000 times higher than that below threshold (Supplementary Information, section D). In addition, the slope efficiency is 8% and the laser efficiency is 4% without any p–i–n diodes (Supplementary Information, section E). The resolution limit of the monochromator (~100 pm) is much larger than the linewidth of the even nanocavity mode (~1 pm) and, thus, linewidth narrowing relative to the lasing could not be detected. We separately confirmed that sample heating due to increasing pump powers is negligible (see Supplementary Information, section F, for temperature dependence). Figure 4b and Fig. 4c show near-infrared camera images of the nanocavity below and above the threshold power, respectively. Figure 4d, e shows images of a waveguide facet, demonstrating that a portion of the Raman laser beam was successfully extracted from the even-mode extraction waveguide.

This low-threshold lasing result is a consequence of the fact that our nanocavity design produces net Raman gain in the low-excitation range before TPA-induced FCA becomes dominant. Because Raman gain has a linear dependence on pump power whereas TPA-induced FCA has a superlinear dependence, the Raman gain can exceed losses for low pump power in our design, where the high Q_R value and the large overlap between the nanocavity modes have especially important roles. Although the lasing output power gradually saturates with increasing pump power, most probably as a result of TPA-induced FCA, this effect could be reduced by reducing the free carrier lifetimes. There is also potential for further performance enhancement, including the reduction of threshold pump power ($\lesssim$100 nW), for example by increasing the Q_P and Q_R factors[23] and modifying the volumes. Such an ultralow threshold is encouraging for a number of reasons. For instance, electrically driven silicon spontaneous-emission sources might be used for integrated pump light sources even though their efficiencies would be low, and Raman silicon laser chips without external pump sources could be realized in the future. The operational wavelength range could be extended above and below the 1.55-μm band[25]. It will also be possible to make other Raman amplification devices based on photonic crystals[26–28] using our design strategy. We believe that our device will stimulate silicon photonics research in a number of areas for the realization of compact photonic integrated circuit chips.

METHODS SUMMARY

We used the three-dimensional, finite-difference time-domain method[29] to calculate the band structure and the electric field distributions in Fig. 1, where the structural parameters in Fig. 2a were used. The calculated Q_P and Q_R values are 500,000 and 4,000,000, respectively. The experimental Q values obtained from Fig. 3b, c are smaller owing to the load of the two adjacent waveguides and imperfections in the fabricated samples[29,30].

The samples were fabricated using the following steps[25]. A thin film of electron-beam resist was deposited by spin coating. The photonic-crystal patterns were drawn on the resist by electron-beam lithography. Next the samples were immersed in the developer at room temperature (22 °C) and the developed mask patterns were transferred to the top silicon slab using sulphur-hexafluoride-based dry etching. Finally the silicon dioxide layer underneath the patterned region was selectively removed using hydrofluoric acid to form an air-bridge structure.

In the optical measurements, the temperature of the sample stage was stabilized at room temperature using a Peltier controller. The nanocavity modes were excited by evanescent mode coupling with the corresponding waveguides, and dropped light from the nanocavity in the direction vertical to the slab was measured while scanning the wavelength-tuneable laser with a narrow linewidth. The signal was collected from the 5-μm spot area at the centre of the nanocavity as shown in Fig. 2a. This measurement configuration is convenient for performing sensitive, quantitative analysis of the Raman laser (Supplementary Information, section E). The odd-mode excitation waveguide was fabricated close to the nanocavity because the E_{y_pump} distribution is tightly confined in the y direction (Fig. 1g). For high-sensitivity Raman spectroscopy, we used a 500-mm-focal-length monochromator

with a liquid-nitrogen-cooled InGaAs-arrayed detector and a 0.65-numerical-aperture objective lens for the dropped light.

Received 21 February; accepted 30 April 2013.

1. Liu, A. *et al.* A high-speed silicon optical modulator based on a metal–oxide–semiconductor capacitor. *Nature* **427,** 615–618 (2004).
2. Jalali, B. & Fathpour, S. Silicon photonics. *J. Lightwave Technol.* **24,** 4600–4615 (2006).
3. Barkai, A. *et al.* Integrated silicon photonics for optical networks. *J. Opt. Netw.* **6,** 25–47 (2007).
4. Fang, A. W. *et al.* Hybrid silicon evanescent devices. *Mater. Today* **10,** 28–35 (2007).
5. Won, R. Integrating silicon photonics. *Nature Photon.* **4,** 498–499 (2010).
6. Michel, J., Liu, J. & Kimerling, L. C. High-performance Ge-on-Si photodetectors. *Nature Photon.* **4,** 527–534 (2010).
7. Claps, R., Dimitropoulos, D., Han, Y. & Jalali, B. Observation of Raman emission in silicon waveguides at 1.54 μm. *Opt. Express* **10,** 1305–1313 (2002).
8. Claps, R., Dimitropoulos, D., Raghunathan, V., Han, Y. & Jalali, B. Observation of stimulated Raman amplification in silicon waveguides. *Opt. Express* **11,** 1731–1739 (2003).
9. Boyraz, O. & Jalali, B. Demonstration of a silicon Raman laser. *Opt. Express* **12,** 5269–5273 (2004).
10. Rong, H. *et al.* An all-silicon Raman laser. *Nature* **433,** 292–294 (2005).
11. Rong, H. *et al.* A continuous-wave Raman silicon laser. *Nature* **433,** 725–728 (2005).
12. Rong, H. *et al.* Low-threshold continuous-wave Raman silicon laser. *Nature Photon.* **1,** 232–237 (2007).
13. Yang, X. & Wong, C. W. Design of photonic band gap nanocavities for stimulated Raman amplification and lasing in monolithic silicon. *Opt. Express* **13,** 4723–4730 (2005).
14. Yang, X. & Wong, C. W. Coupled-mode theory for stimulated Raman scattering in high-Q/V_m silicon photonic band gap defect cavity lasers. *Opt. Express* **15,** 4763–4780 (2007).
15. Loudon, R. The Raman effect in crystals. *Adv. Phys.* **13,** 423–482 (1964).
16. Ralston, J. M. & Chang, R. K. Spontaneous-Raman-scattering efficiency and stimulated scattering in silicon. *Phys. Rev. B* **2,** 1858–1862 (1970).
17. Liang, T. K. & Tsang, H. K. Role of free carriers from two-photon absorption in Raman amplification in silicon-on-insulator waveguides. *Appl. Phys. Lett.* **84,** 2745–2747 (2004).
18. Claps, R., Raghunathan, V., Dimitropoulos, D. & Jalali, B. Influence of nonlinear absorption on Raman amplification in silicon waveguides. *Opt. Express* **12,** 2774–2780 (2004).
19. Noda, S., Chutinan, A. & Imada, M. Trapping and emission of photons by a single defect in a photonic bandgap structure. *Nature* **407,** 608–610 (2000).
20. Akahane, Y., Asano, T., Song, B. S. & Noda, S. High-*Q* photonic nanocavity in a two-dimensional photonic crystal. *Nature* **425,** 944–947 (2003).
21. Song, B. S., Noda, S., Asano, T. & Akahane, Y. Ultra-high-*Q* photonic double-heterostructure nanocavity. *Nature Mater.* **4,** 207–210 (2005).
22. Takahashi, Y. *et al.* Design and demonstration of high-*Q* photonic heterostructure nanocavities suitable for integration. *Opt. Express* **17,** 18093–18102 (2009).
23. Taguchi, Y., Takahashi, Y., Sato, Y., Asano, T. & Noda, S. Statistical studies of photonic heterostructure nanocavities with an average *Q* factor of three million. *Opt. Express* **19,** 11916–11921 (2011).
24. Takano, H., Asano, T. & Noda, S. at *Spring Meeting Jpn Soc. Appl. Phys.*, abstr. 29a-ZB-8 (2007).
25. Terawaki, R., Takahashi, Y., Chihara, M., Inui, Y. & Noda, S. Ultrahigh-Q photonic crystal nanocavities in wide optical telecommunication bands. *Opt. Express* **20,** 22743–22752 (2012).
26. Song, B. S., Jeon, S. B. & Noda, S. Symmetrically glass-clad photonic crystal nanocavities with ultrahigh quality factors. *Opt. Lett.* **36,** 91–93 (2011).
27. Han, Z., Checoury, X., Haret, L.-D. & Boucaud, P. High quality factor in a two-dimensional photonic crystal cavity on silicon-on-insulator. *Opt. Lett.* **36,** 1749–1751 (2011).
28. Baba, T. Slow light in photonic crystals. *Nature Photon.* **2,** 465–473 (2008).
29. Hagino, H., Takahashi, Y., Tanaka, Y., Asano, T. & Noda, S. Effects of fluctuation in air hole radii and positions on optical characteristics in photonic crystal heterostructure nanocavities. *Phys. Rev. B* **79,** 085112 (2009).
30. Asano, T., Song, B. S. & Noda, S. Analysis of the experimental *Q* factors (~1 million) of photonic crystal nanocavities. *Opt. Express* **14,** 1996–2002 (2006).

Supplementary Information is available in the online version of the paper.

Acknowledgements We especially thank H. Takano for a preliminary calculation done before the start of this project. We thank K. Ishizaki and K. Kitamura for assistance in device fabrication, Y. Tanaka for assistance with finite-difference time-domain calculations, A. Oskooi and H. Ishihara for comments, and Y. Sakamoto for software assistance. Y.T. is supported by the NanoSquare programme, Funds for the Development of Human Resources in Science and Technology, commissioned by MEXT. This work was supported by JST, PRESTO, the NanoSquare programme and MEXT KAKENHI (grant numbers 23104721 and 21104512). The spectral measurements were partly supported by JSPS KAKENHI (grant number 23686015) and the Asahi Grass Foundation. The device fabrication was greatly supported by JSPS KAKENHI (grant number 20226002), the Ministry of Economy, Trade and Industry (METI) through its 'Future Pioneering Projects', and the CPHoST programme.

Author Contributions Y.T. designed the project, designed the original device, fabricated the samples, performed the measurements and wrote the paper. S.N. organized the contribution to the project from Kyoto University, where the fundamental studies to realize high-*Q*/*V* nanocavities and the initial investigation into Raman lasers was performed. S.N. also contributed greatly to writing the paper. Y.I. analytically determined the optimum crystalline direction for lasing and contributed to writing Supplementary Information, sections A and B. M.C. established the method to tune the nanocavity mode spacing, T.A. contributed to the theoretical analysis and R.T. contributed to the development of the measurement system.

Author Information Reprints and permissions information is available at www.nature.com/reprints. The authors declare no competing financial interests. Readers are welcome to comment on the online version of the paper. Correspondence and requests for materials should be addressed to Y.T. (y-takahashi@21c.osakafu-u.ac.jp) or S.N. (snoda@kuee.kyoto-u.ac.jp).